Macroscopic description of nonequilibrium effects in thermal transpiration flows in annular microchannels

Peyman Taheri and Majid Bahrami
Laboratory for Alternative Energy Conversion (LAEC), School of Engineering Science, Mechatronic Systems Engineering, Simon Fraser University, Surrey, British Columbia, Canada V3T 0A3
(Received 20 May 2012; published 17 September 2012)

Thermal transpiration flow of rarefied gases in annular channels is considered where the driving force for the flow is a temperature gradient applied in the channel walls. The influence of gas rarefaction, aspect ratio of the annulus, and surface accommodation coefficient on mass and heat transfer in the process are investigated. An analytical approach to the problem is conducted based on linearized Navier-Stokes-Fourier (NSF) and regularized 13-moment (R13) equations, and a closed-form expression for Knudsen boundary layers is obtained. The results are compared to available solutions of the Boltzmann equation to highlight the advantages of the R13 over the NSF equations in describing nonequilibrium effects in this particular thermally driven flow. Through comparisons with kinetic data, it is shown that R13 equations are valid for moderate Knudsen numbers, i.e., Kn < 0.5 where NSF equations fail to describe the flow fields properly.

DOI: 10.1103/PhysRevE.86.036311 PACS number(s): 47.10.ab, 47.10.ad, 51.10.+y, 47.45.−n

I. INTRODUCTION

In a rarefied gas confined in a channel or a pipe, when a temperature gradient is applied on the walls, a flow is induced in the direction of the temperature gradient, i.e., from cold to hot [1,2]. This pure thermally induced flow, initiates within a thin layer adjacent to the walls. However, as a result of shear-stress diffusion, the thickness of this layer grows, and the flow eventually fills the width of the channel or pipe if its length is sufficiently large. This phenomenon was first reported by Reynolds [3] in 1879 who named it *thermal transpiration flow*. At the same time, Maxwell [4] was trying to provide a microscopic description for this problem using the kinetic theory of gases. Later, experimental observations by Knudsen [5,6] proved the existence of a pumping effect in thermally driven flows, the so-called *thermomolecular pressure difference* [7–12]. Recently, the possibility of using the pumping effect of thermal transpiration to create a microcompressor without moving parts (Knudsen compressor) has motivated rigorous experimental studies [13–15].

In gaseous flows, the measure for gas rarefaction is the Knudsen number $\mathrm{Kn} = \lambda/\ell$, where the ratio of the molecular mean free path is λ, and the geometric characteristic length of the flow is ℓ. Accordingly, rarefied conditions (large Knudsen numbers) are common in microsettings as well as in low-density (near vacuum) flows. Since, in rarefied gas flows, there are not sufficient collisions between the gas particles, an equilibrium state cannot be maintained, and the arising nonequilibrium effects alter the transport fields of mass and heat. Furthermore, since collisions between the gas molecules and the solid wall are different from intermolecular collisions, a nonequilibrium layer known as the Knudsen boundary layer forms adjacent to the solid surface, which extends to a distance of about two to three mean free paths. It is evident that, for nonequilibrium gas flows, the well established equations of classical fluid dynamics, i.e., Navier-Stokes and Fourier (NSF) equations, cease to be valid [16]. Consequently, nonequilibrium transport processes, including thermal transpiration flow, are mostly investigated numerically through kinetic models using the Boltzmann equation.

Thermal transpiration between two parallel plates is a well-known problem in kinetic theory, for which kinetic solutions obtained from the Bhatnagar-Gross-Krook (BGK) model are reported in Refs. [17–21]. For this fundamental problem, more realistic kinetic data based on a linearized Boltzmann (LB) equation are also available in Refs. [22,23]. For circular channels, kinetic simulations of thermal transpiration were initiated by Sone and Yamamoto [24] and Loyalka [25] in 1968. Due to the popularity of tubular flow passages in practical applications, their work was extended to study the effects of surface accommodation on mass and heat transfer in thermally induced flows of monatomic and polyatomic gases [26–31]. An extensive bibliography and careful comparison of kinetic solutions for thermal transpiration is available in Ref. [32].

Although kinetic solutions are very accurate, their complexity and computational cost limit their application, particularly in the engineering community. As alternatives to kinetic approaches, extended macroscopic transport equations, which are derived from the Boltzmann equation, can be used to describe rarefied gas flows at lower computational cost than the Boltzmann equation itself [33]. This is performed by reducing the degrees of freedom of the velocity distribution function, which is the main variable in the kinetic equation, to the degrees of freedom of a finite set of macroscopic variables. Grad's moment expansion [34,35] and the Chapman-Enskog expansion [36] are the classical methods to extract hydrodynamic-like equations from the Boltzmann equation.

In the present paper, regularized 13-moment (R13) equations are used to describe the thermal transpiration flow of moderately rarefied gases in an annulus between two concentric cylinders. The R13 system is a regularized version of the classical Grad's 13-moment equations [16,37,38], suitable for flow simulation in the transition regime $\mathrm{Kn} \leqslant 1$, the regime in which the flow is dominated with Knudsen layers [39]. In contrast to Grad's 13-moment system, the R13 equations yield smooth shock structures over a wide range of Mach

numbers [40] and correctly predict the formation of *Knudsen boundary layers* in fundamental boundary value problems for microflows [12,41–45]. Knudsen boundary layers are common rarefaction (nonequilibrium) effect in low-speed rarefied gas flows.

Annular channels are considered in this paper due to their specific geometrical property. When the aspect ratio of the annulus (ratio of the inner cylinder radius to outer cylinder radius) is zero, the problem represents thermal transpiration in tubes, and for annuli with aspect ratios close to unity, the problem represents thermal transpiration in parallel plate channels.

In the following, linearized R13 equations and their boundary conditions [46] are adopted to describe thermally induced flows in annular flow passages. Since experimental data for the considered problem are not available, analytical solutions for linearized R13 and Navier-Stokes-Fourier (NSF) equations are obtained and are compared to some accurate kinetic data [47]. Through comparisons, it is shown that, due to the capability of the R13 equations in capturing of rarefaction effects, which are missing in the NSF solutions, the R13 results match better with kinetic data. Our compact analytical solutions, which required modest computational effort, revealed that the presence of Knudsen boundary layers in the R13 solutions and their contributions to mass and heat transfer were the main reasons for this improvement.

II. FORMULATION OF THE PROBLEM

Monatomic ideal gases are considered with $p = \rho\theta$ as the equation of state in which p, ρ, and $\theta = RT$ are pressure, mass density, and temperature in energy units (J kg^{-1}), respectively. The gas constant is R, and T is the absolute temperature.

The flow configuration is shown in Fig. 1. The gas, confined in the annulus between two stationary coaxial cylinders, flows axially as a result of temperature variation along the cylindrical walls, i.e., *thermal transpiration flow*. Suggested by the channel geometry, it is appropriate to use cylindrical coordinates $\mathbf{x} = \{r,\varphi,z\}$ as shown in Fig. 1.

The pressure along the channel is a constant p_0. The wall temperature at the inlet and outlet of the channel are $\theta_1^{\rm w}$ and $\theta_2^{\rm w}$, respectively, with $\theta_1^{\rm w} < \theta_2^{\rm w}$. The superscript "w" refers to the properties at the cylindrical walls. The temperature distribution

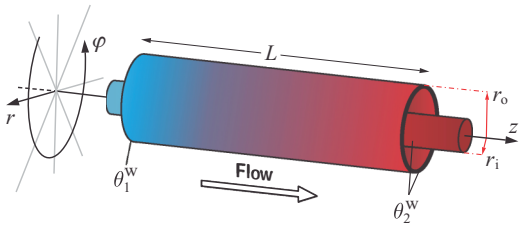

FIG. 1. (Color online) Cylindrical coordinates and flow configuration in thermal transpiration flow between two coaxial cylinders of length L. The flow is driven by a constant temperature gradient in the axial direction, applied on both cylinders. Wall temperatures at the ends of the channel are $\theta_1^{\rm w}$ and $\theta_2^{\rm w}$ with $\theta_2^{\rm w} > \theta_1^{\rm w}$. The annular gap size is $\Delta r = r_{\rm o} - r_{\rm i}$, and the annulus aspect ratio is $\varepsilon = r_{\rm i}/r_{\rm o}$.

in the walls is $\theta^{\rm w}(z) = \theta_1^{\rm w} + \alpha z$, where $\alpha = (\theta_2^{\rm w} - \theta_1^{\rm w})/L$ is a positive and constant temperature gradient in the axial direction. The inner and outer radii of the circular gap are $r_{\rm i}$ and $r_{\rm o}$, respectively. The aspect ratio of the annulus is $\varepsilon = r_{\rm i}/r_{\rm o}$, and the gap size is $\Delta r = r_{\rm o} - r_{\rm i}$. The length of the flow passage L is assumed to be significantly large compared to its radial dimension, $L \gg \Delta r$, thus, boundary effects at the entry and exit can be neglected, and the established temperature gradient in the gas and channel walls is the same.

At this configuration, a pure thermally driven flow occurs from the cold side of the channel to the hot side. We investigate steady-state flow of the gas in the absence of external force (e.g., gravity), driven by a constant and small temperature gradient in the z direction. Since the cylinders are not rotating, the flow is irrotational $v_\varphi = 0$ and independent of the azimuthal direction $\partial/\partial_\varphi = 0$.

It must be pointed out that, due to compressibility effects, the actual transpiration flow in the annulus is a two-dimensional problem in the r-z plane, which requires a numerical approach. Nevertheless, it is shown through kinetic simulations that, for low Mach number flows through long capillaries, one can safely use "linear analysis" to discard the axial compressibility effects and to simplify the problem such that a one-dimensional analysis suffices to investigate the local distribution of flow properties across the channel [12,32,44]. As discussed in Ref. [44], it is straightforward to show that a nonzero radial velocity v_r is a nonlinear phenomenon due to compressibility effects, thus, in our linear analysis, $v_r = 0$ is considered.

III. REGULARIZED 13-MOMENT EQUATIONS IN LINEAR FORM

The derivations of regularized 13-moment (R13) equations and their corresponding boundary conditions for channel flows are discussed in Refs. [37,46]. The transformed equations and boundary conditions in cylindrical coordinates are presented in Ref. [12]; details on the transformation are available in Ref. [48].

In the present paper, in order to obtain closed-form analytical solutions, linearized and steady-state equations are considered. For linearization, we consider a reference equilibrium state defined by p_0, $\theta_0 = (\theta_1^{\rm w} + \theta_2^{\rm w})/2$, and $\rho_0 = p_0/\theta_0$ in which the gas is at rest, $\mathbf{v}_0 = 0$, and in equilibrium, i.e., $\mathbf{q}_0 = \boldsymbol{\sigma}_0 = 0$. The vectors $\mathbf{v}$ and $\mathbf{q}$ correspond to velocity and heat flux, whereas, $\boldsymbol{\sigma}$ is the stress tensor deviator tensor.

The core equations in the R13 system are the main conservation laws for mass, momentum, and energy densities, which, for the considered problem in steady-state and linearized forms, read

$$\boldsymbol{\nabla}\cdot\mathbf{v} = 0, \tag{1}$$

$$\boldsymbol{\nabla}\cdot\boldsymbol{\sigma} = 0, \tag{2}$$

$$\boldsymbol{\nabla}\cdot\mathbf{q} = 0. \tag{3}$$

In the R13 system, stress deviator tensor $\boldsymbol{\sigma}$ and heat-flux vector $\mathbf{q}$ are given by their respective moment equations

[16,37] that again, in steady-state and linearized forms, are

$$\frac{4}{5}\langle\nabla\mathbf{q}\rangle+\nabla\cdot\mathbf{m}=-2p_0\langle\nabla\mathbf{v}\rangle-\frac{p_0}{\mu_0}\boldsymbol{\sigma}, \tag{4}$$

$$\theta_0\nabla\cdot\boldsymbol{\sigma}+\frac{1}{2}\nabla\cdot\mathbf{R}=-\frac{5}{2}p_0\nabla\theta-\mathrm{Pr}\,\frac{p_0}{\mu_0}\mathbf{q}. \tag{5}$$

Here, μ_0 is the viscosity of the gas at the reference (equilibrium) state, and Pr is the Prandtl number.

Closure for Eqs. (1)–(5) is obtained from regularization [16,37] and leads to constitutive relations for higher-order moments $\mathbf{R}$ and $\mathbf{m}$, which, in linear form, read

$$\mathbf{R}=-A\frac{\mu_0}{\rho_0}\langle\nabla\mathbf{q}\rangle, \tag{6}$$

$$\mathbf{m}=-B\frac{\mu_0}{\rho_0}\langle\nabla\boldsymbol{\sigma}\rangle. \tag{7}$$

In the above equations, the terms inside the angular brackets $\langle\cdots\rangle$ indicate the trace-free part of the symmetric tensors. For instance, the trace-free part of the symmetric velocity gradient reads

$$\langle\nabla\mathbf{v}\rangle=\frac{1}{2}[\nabla\mathbf{v}+(\nabla\mathbf{v})^{\mathrm{T}}]-\frac{1}{3}(\nabla\cdot\mathbf{v})\mathbf{I}, \tag{8}$$

where the superscript "T" indicates the transposed tensor and $\mathbf{I}$ is the unit tensor. For the trace-free part of rank-3 tensors, see Appendix A in Ref. [16].

The Prandtl number (Pr) in the moment equation for heat flux and the coefficients A and B in the constitutive equations are different in the BGK kinetic model and the linearized Boltzmann equation for Maxwellian molecules [16]. For the BGK kinetic model, these coefficients are

$$\mathrm{Pr}^{\mathrm{BGK}}=1,\qquad A^{\mathrm{BGK}}=\frac{28}{5},\qquad B^{\mathrm{BGK}}=3, \tag{9}$$

whereas, for the LB equation, they read

$$\mathrm{Pr}^{\mathrm{LB}}=\frac{2}{3},\qquad A^{\mathrm{LB}}=\frac{24}{5},\qquad B^{\mathrm{LB}}=2. \tag{10}$$

In the hydrodynamics limit where the high-order moments $\mathbf{R}$ and $\mathbf{m}$ vanish, the terms on the left-hand side of Eqs. (4) and (5) are zero, and they reduce to the linearized Navier-Stokes and Fourier laws of classical hydrodynamics, that is, Newtonian viscous shear and Fourier's heat conduction,

$$\boldsymbol{\sigma}=-2\mu_0\langle\nabla\mathbf{v}\rangle, \tag{11}$$

$$\mathbf{q}=-\kappa_0\nabla\theta. \tag{12}$$

with $\kappa_0=5\mu_0/(2\ \mathrm{Pr})$ as the thermal conductivity coefficient for ideal gas at the reference state. Equations (11) and (12) along with the conservation laws (1)–(3) form the linearized Navier-Stokes-Fourier system,

$$\nabla\cdot\mathbf{v}=0,\qquad \nabla^2\mathbf{v}=0,\qquad \nabla^2\theta=0. \tag{13}$$

IV. WALL BOUNDARY CONDITIONS

For the considered boundary value problem, wall boundary conditions are required to relate properties of the gas (adjacent to the wall) to the wall temperature and the wall velocity. Since R13 equations are derived from the Boltzmann equation, it is natural to base the derivation of their boundary conditions on the boundary condition for the Boltzmann equation. Detailed discussion on the derivation of wall boundary conditions for R13 equations is available in Refs. [46,48] where macroscopic boundary conditions for high-order moments are derived from Maxwell's boundary condition for the Boltzmann equation [4].

A. Boundary conditions for the regularized 13-moment equations

The required boundary conditions for the R13 system in linearized form are [44,46,48,49]

$$\sigma_{tn}=\frac{\chi}{2-\chi}\sqrt{\frac{2}{\pi\theta_0}}\left(-p_0V_t-\frac{1}{5}q_t-\frac{1}{2}m_{tnn}\right), \tag{14}$$

$$R_{tn}=\frac{\chi}{2-\chi}\sqrt{\frac{2}{\pi\theta_0}}\left(p_0\theta_0V_t-\frac{11}{5}\theta_0q_t-\frac{1}{2}\theta_0m_{tnn}\right). \tag{15}$$

The subscripts "t" and "n" indicate *tangential* and *normal* directions with respect to the wall, that is, the z and r directions, respectively [cf. Fig. 1]. The wall normal points in the radial direction toward the gas, thus, wall normal vectors have opposite signs on the inner and outer cylinders. Slip velocity on the wall is denoted by V_t and

$$V_t=v_t-v_t^{\mathrm{w}}. \tag{16}$$

The kinetic between the gas particles and the wall surface is reflected in the surface accommodation coefficient χ, where $\chi=0$ and $\chi=1$ describe fully reflective (smooth) and fully diffusive (rough) walls, respectively.

As discussed in Ref. [44], additional boundary conditions for temperature, density, and normal components of heat flux and stress are required for the nonlinear R13 equations. Since, in the present paper, we consider the linearized problem only, the boundary conditions required for the nonlinear setting are not shown.

B. Slip condition for Navier-Stokes-Fourier equations

The Chapman-Enskog expansion of the quantities in boundary conditions (14) and (15) allows identifying their high-order terms. This general strategy is introduced in Ref. [50] to obtain a second-order velocity-slip condition for the NSF system. In Appendix C of Ref. [48], this strategy was extended to derive the second-order slip condition for curved boundaries. For axial flows in cylindrical coordinates, the slip boundary condition in linear form reads [12]

$$V_z^{\mathrm{NSF}}=-\frac{2-\chi}{\chi}\sqrt{\frac{\pi\theta_0}{2}}\frac{\sigma_{rz}^{\mathrm{NSF}}}{p_0}n_r-\frac{1}{5}\frac{q_z^{\mathrm{NSF}}}{p_0}+\left[\left(\frac{1}{5\,\mathrm{Pr}}+\frac{4B}{15}\right)\times\frac{\partial\sigma_{rz}^{\mathrm{NSF}}}{\partial r}+\left(\frac{1}{5\ \mathrm{Pr}}-\frac{B}{15}\right)\frac{\sigma_{rz}^{\mathrm{NSF}}}{r}\right]\frac{\mu_0\theta_0}{p_0^2}. \tag{17}$$

The quantities $\sigma_{rz}^{\mathrm{NSF}}$ and q_z^{NSF} are the Navier-Stokes shear-stress Eq. (11) and Fourier's heat conduction Eq. (12). The first and second terms represent the first-order slip velocity, and the rest are second-order corrections. The term $\boldsymbol{\sigma}_{rz}^{\mathrm{NSF}}/r$ accounts for the curvature effect of the channel wall. The wall normal is indicated by n_r with $n_r=+1$ for the inner wall and $n_r=-1$ for the outer wall.

V. FLOW EQUATIONS

Flow equations for thermal transpiration in annular channels are obtained by transforming Eqs. (1)–(7) and the NSF equations [cf. Eq. (13)] into cylindrical coordinates. Details on the transformation are available in Ref. [48]. For the considered flow configuration, as discussed in Sec. II, the velocity vector $\mathbf{v}$, the heat-flux vector $\mathbf{q}$, and the stress tensor $\boldsymbol{\sigma}$ simplify to

$$\mathbf{v} = \begin{pmatrix} 0 \\ 0 \\ v_z(r) \end{pmatrix}, \quad \mathbf{q} = \begin{pmatrix} q_r(r) \\ 0 \\ q_z(r) \end{pmatrix}, \quad \boldsymbol{\sigma} = \begin{pmatrix} \sigma_{rr}(r) & 0 & \sigma_{rz}(r) \\ 0 & \sigma_{\varphi\varphi}(r) & 0 \\ \sigma_{rz}(r) & 0 & \sigma_{zz}(r) \end{pmatrix}, \tag{18}$$

where all components only depend on the radial coordinate r. Since the stress tensor is trace free, we have $\boldsymbol{\sigma}_{\varphi\varphi} = -\boldsymbol{\sigma}_{rr} - \boldsymbol{\sigma}_{zz}$, that confirms flow is completely independent of the φ direction.

The reference (equilibrium) state properties $\{p_0, \rho_0, \theta_0\}$ and an arbitrary length scale ℓ can be used to define dimensionless quantities. The radial and axial coordinates are normalized with respect to the length scale,

$$\tilde{r} = \frac{r}{\ell}, \qquad \tilde{z} = \frac{z}{\ell}. \tag{19}$$

The remaining variables in dimensionless form are defined as

$$\tilde{\rho} = \frac{\rho}{\rho_0}, \quad \tilde{\theta} = \frac{\theta}{\theta_0}, \quad \tilde{p} = \frac{p}{p_0}, \quad \tilde{\mathbf{v}} = \frac{\mathbf{v}}{\sqrt{\theta_0}}, \quad \tilde{\mathbf{q}} = \frac{\mathbf{q}}{p_0\sqrt{\theta_0}}, \quad \tilde{\sigma} = \frac{\boldsymbol{\sigma}}{p_0}, \quad \tilde{\mathbf{R}} = \frac{\mathbf{R}}{p_0\theta_0}, \quad \tilde{\mathbf{m}} = \frac{\mathbf{m}}{p_0\sqrt{\theta_0}}. \tag{20}$$

The isothermal speed of sound $\sqrt{\theta_0}$ is used to scale the velocity. The tilde signs indicate dimensionless quantities.

The application of differential operators (divergences and gradients) in cylindrical geometry [48] and then, the introduction of the above dimensionless quantities in Eqs. (1)–(7) yield the dimensionless form of the linearized R13 equations in cylindrical coordinates,

$$\left(\frac{\partial}{\partial\tilde{r}} + \frac{1}{\tilde{r}}\right)\tilde{\sigma}_{rz} = 0, \tag{21}$$

$$\frac{1}{2}\left(\frac{\partial}{\partial\tilde{r}} + \frac{1}{\tilde{r}}\right)\tilde{R}_{rz} = -\frac{\mathrm{Pr}}{\mathrm{Kn}}\tilde{q}_z - \frac{5}{2}\tau, \tag{22}$$

$$\frac{2}{5}\frac{\partial\tilde{q}_z}{\partial\tilde{r}} + \frac{\partial\tilde{m}_{rrz}}{\partial\tilde{r}} + \frac{\tilde{m}_{rrz} - \tilde{m}_{\varphi\varphi z}}{\tilde{r}} = -\frac{1}{\mathrm{Kn}}\tilde{\sigma}_{rz} - \frac{\partial\tilde{v}_z}{\partial\tilde{r}}, \tag{23}$$

where τ is the dimensionless temperature gradient along the axial direction (a positive quantity for the flow setting in Fig. 1),

$$\tau = \frac{\ell}{\theta_0}\frac{\partial\theta}{\partial z} = \frac{\partial\tilde{\theta}}{\partial\tilde{z}}. \tag{24}$$

In the dimensionless equations, the reference viscosity μ_0 can be related to the reference molecular mean free path λ_0. Accordingly, the Knudsen number (Kn) appears in the dimensionless equations as

$$\mathrm{Kn} = \frac{\lambda_0}{\ell} \quad \text{with} \quad \lambda_0 = \frac{\mu_0\sqrt{\theta_0}}{p_0}. \tag{25}$$

The Knudsen number is a measure for gas rarefaction.

Equation (21) is the linearized and dimensionless momentum balance [Eq. (2)] in the axial direction. Equation (22) is the axial component of the heat-flux balance [Eq. (5)] in linearized dimensionless form. Equation (23) is the tangential component of shear-stress balance [Eq. (4)]. The dimensionless high-order moments in Eqs. (22) and (23) follow from Eqs. (6) and (7) as

$$\tilde{R}_{rz} = -\frac{1}{2}A\ \mathrm{Kn}\frac{\partial\tilde{q}_z}{\partial\tilde{r}}, \quad \tilde{m}_{rrz} = -\tilde{m}_{\varphi\varphi z} = \frac{2}{3}B\ \mathrm{Kn}\frac{\tilde{\boldsymbol{\sigma}}_{rz}}{\tilde{r}}. \tag{26}$$

Note that, in this flow setting, $\tilde{m}_{rrz}$ and $\tilde{m}_{\varphi\varphi z}$ are geometric curvature effects since they do not appear in transpiration flow analysis through planar channels [43].

The required boundary conditions for the problem are the same as in Eqs. (14) and (15) that, in dimensionless form and with proper coordinate-indicative indices, read

$$\tilde{\boldsymbol{\sigma}}_{rz} = \frac{\chi}{2-\chi}\sqrt{\frac{2}{\pi}}\left(-\tilde{V}_z - \frac{1}{5}\tilde{q}_z - \frac{1}{2}\tilde{m}_{rrz}\right)n_r, \tag{27}$$

$$\tilde{R}_{rz} = \frac{\chi}{2-\chi}\sqrt{\frac{2}{\pi}}\left(\tilde{V}_z - \frac{11}{5}\tilde{q}_z - \frac{1}{2}\tilde{m}_{rrz}\right)n_r. \tag{28}$$

As mentioned in Sec. III, in the asymptotic limit of $\mathrm{Kn} \to 0$, the balance equations for stress and heat flux [Eqs. (4) and (5)] reduce to Newtonian viscous shear and Fourier's heat conduction, respectively, which, in linearized dimensionless form in cylindrical coordinates, are

$$\tilde{\sigma}_{rz}^{\mathrm{NSF}} = -\mathrm{Kn}\frac{\partial\tilde{v}_z}{\partial\tilde{r}}, \qquad \tilde{q}_z^{\mathrm{NSF}} = -\frac{5}{2}\frac{\mathrm{Kn}}{\mathrm{Pr}}\frac{\partial\tilde{\theta}}{\partial\tilde{z}}. \tag{29}$$

Replacement of the above equations in Eqs. (21)–(23) and setting $\tilde{R}_{rz} = \tilde{m}_{rrz} = \tilde{m}_{\varphi\varphi z} = 0$ gives the NSF equations for this problem, i.e.,

$$\left(\frac{\partial}{\partial\tilde{r}} + \frac{1}{\tilde{r}}\right)\frac{\partial\tilde{v}_z}{\partial\tilde{r}} = 0. \tag{30}$$

Note that Eqs. (22) and (23) are automatically satisfied.

The required boundary condition for Eq. (30) is the slip condition (17) in dimensionless form

$$\tilde{V}_z^{\mathrm{NSF}} = \left(\frac{2-\chi}{\chi}\sqrt{\frac{\pi}{2}}\frac{\partial\tilde{v}_z}{\partial\tilde{r}}n_r + \frac{1}{2\,\mathrm{Pr}}\tau\right)\mathrm{Kn} - \left[\left(\frac{1}{5\,\mathrm{Pr}} + \frac{4B}{15}\right)\times\frac{\partial^2\tilde{v}_z}{\partial\tilde{r}^2} + \left(\frac{1}{5\,\mathrm{Pr}} - \frac{B}{15}\right)\frac{1}{\tilde{r}}\frac{\partial\tilde{v}_z}{\partial\tilde{r}}\right]\mathrm{Kn}^2. \tag{31}$$

The terms multiplied by Kn^2 are the second-order corrections to slip velocity.

VI. RESULTS AND DISCUSSIONS

A. Analytical solution for regularized 13-moment equation

Replacement of Eq. (26) into Eqs. (22) and (23) and subsequent integration gives the following analytical solutions for shear stress $\tilde{\boldsymbol{\sigma}}_{rz}$, axial heat flux $\tilde{q}_z$, and velocity $\tilde{v}_z$:

$$\tilde{\sigma}_{rz} = \left\{\frac{C_1}{\tilde{r}}\right\}, \tag{32}$$

$$\tilde{q}_z = \left\{-\frac{5}{2}\frac{\mathrm{Kn}}{\mathrm{Pr}}\tau\right\} + C_2 I_0\left(\frac{2}{\mathrm{Kn}}\sqrt{\frac{\mathrm{Pr}}{A}}\tilde{r}\right) + C_3 K_0\left(\frac{2}{\mathrm{Kn}}\sqrt{\frac{\mathrm{Pr}}{A}}\tilde{r}\right), \tag{33}$$

$$\tilde{v}_z = \left\{C_4 + \frac{\mathrm{Kn}}{\mathrm{Pr}}\tau - \frac{C_1}{\mathrm{Kn}}\ln(\tilde{r})\right\} - \frac{2}{5}\left[C_2 I_0\left(\frac{2}{\mathrm{Kn}}\sqrt{\frac{\mathrm{Pr}}{A}}\tilde{r}\right) + C_3 K_0\left(\frac{2}{\mathrm{Kn}}\sqrt{\frac{\mathrm{Pr}}{A}}\tilde{r}\right)\right]. \tag{34}$$

The terms within curly brackets indicate the solution of the NSF equations. In the above general solutions, C_1 to C_4 are the integrating constants that must be determined from the boundary conditions on both inner and outer walls. For the NSF solution, the constants C_1 and C_4 can be obtained from the slip condition (31). For the R13 solution, the required boundary conditions are (27) and (28). The expressions for constants C_1 to C_4 are too bulky, hence, they are not shown here. These constants can be computed using analytical software packages, such as MATHEMATICA or MAPLE. It is important to mention that all constants linearly depend on the axial temperature gradient τ. Details of integrating constants for Poiseuille flows in annular channels are thoroughly discussed in Ref. [45], and a similar analysis can be applied for the considered problem.

As given in Eq. (32), both R13 and NSF systems yield an identical solution for shear stress. Equation (33) confirms that NSF yields heat flow only in the presence of a temperature gradient, whereas, the full R13 solution includes other terms that describe rarefaction effects, i.e., a heat flux which is not driven by temperature gradient. The zeroth-order modified Bessel functions I_0 and K_0 represent the Knudsen boundary layers. The R13 velocity solution shows that Knudsen layers contribute in the flow velocity. This effect is missing in the NSF velocity solution.

For $\chi = 1$, $\varepsilon = 0.1$, and $\mathrm{Kn} = \{0.05, 0.15, 0.3\}$, the dimensionless solutions (32)–(34) are plotted in Fig. 2, which are normalized with respect to the dimensionless temperature gradient τ. The results are obtained for both BGK and LB coefficients as given in Eqs. (9) and (10). The slip condition for the NSF yields $C_1 = 0$. Accordingly, $\tilde{\sigma}_{rz}^{\mathrm{NSF}} = 0$, and the second-order slip condition reduces to

$$\tilde{V}_z^{\mathrm{NSF}} = \frac{1}{2}\frac{\mathrm{Kn}}{\mathrm{Pr}}\tau. \tag{35}$$

Due to this simplification, the effects of accommodation coefficients and second-order slip terms cannot be captured for NSF equations in linear analysis.

Figure 2(a) shows shear-stress distribution in the annular gap between $r_\mathrm{i}/\Delta r = \varepsilon/(1-\varepsilon)$ and $r_\mathrm{o}/\Delta r = 1/(1-\varepsilon)$. In contrast to the NSF, the constant C_1 does not vanish in the R13 solution, and the predicted shear stress is nonzero. However, in the hydrodynamic limit, when $\mathrm{Kn} \to 0$, the R13 shear stress converges to that of the NSF. As the Knudsen number increases, the solutions with LB coefficients yield higher shear stress on the inner wall, compared to BGK coefficients. Unfortunately, kinetic data (solutions of the Boltzmann equation) for shear stress are not reported in the literature to perform a comparison and to evaluate the accuracy of our results.

Figure 2(b) shows the heat-flux distribution across the channel. As given in Eq. (33), the NSF predicts a uniform heat flow in the opposite direction of the temperature gradient, postulated by Fourier's law. For $\mathrm{Kn} = 0.05$, the R13 solution differs from the NSF only on the narrow region close to the boundaries, which is the effect of Knudsen boundary layers, i.e., the terms with Bessel functions. As the Knudsen number increases, the thickness of the Knudsen layers increases; for $\mathrm{Kn} = \{0.15, 0.3\}$, the Knudsen layers affect the whole cross section. The heat flow in the Knudsen layers competes with Fourier heat flow, i.e., it occurs in the direction of the temperature gradient. The magnitude of heat flow predicted

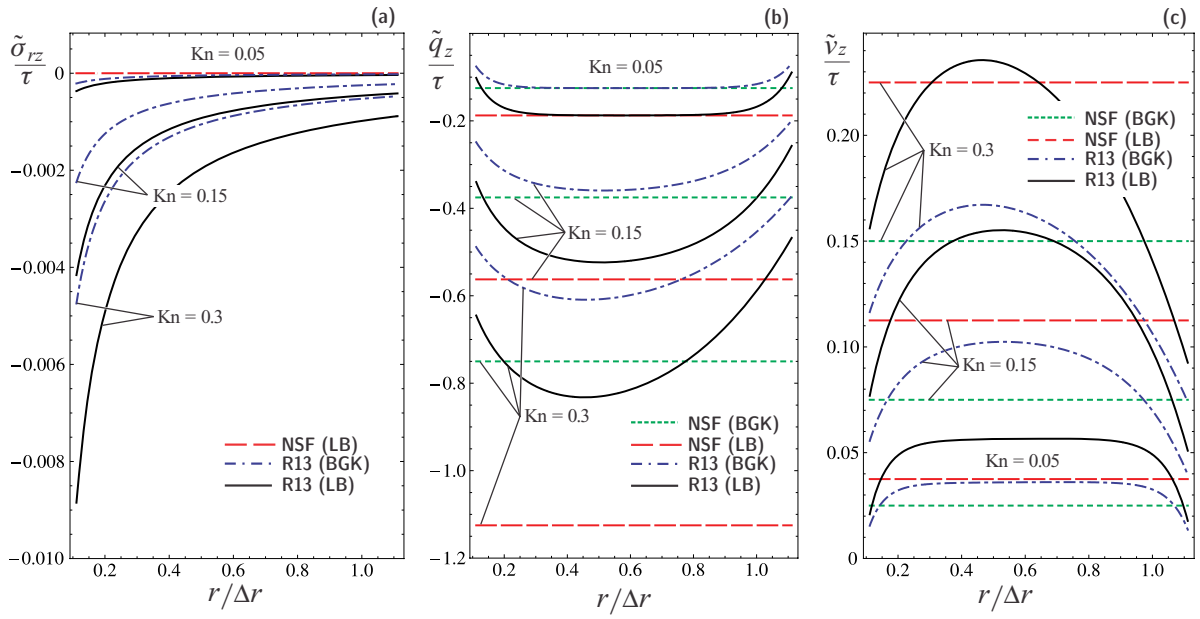

FIG. 2. (Color online) Normalized distributions of (a) shear stress, (b) heat flux, and (c) velocity across the annulus are plotted. The plots are obtained for $\chi = 1$ and $\varepsilon = 0.1$ with both BGK and LB coefficients. Solutions for the NSF and R13 are compared for $\mathrm{Kn} = \{0.05, 0.15, 0.3\}$.

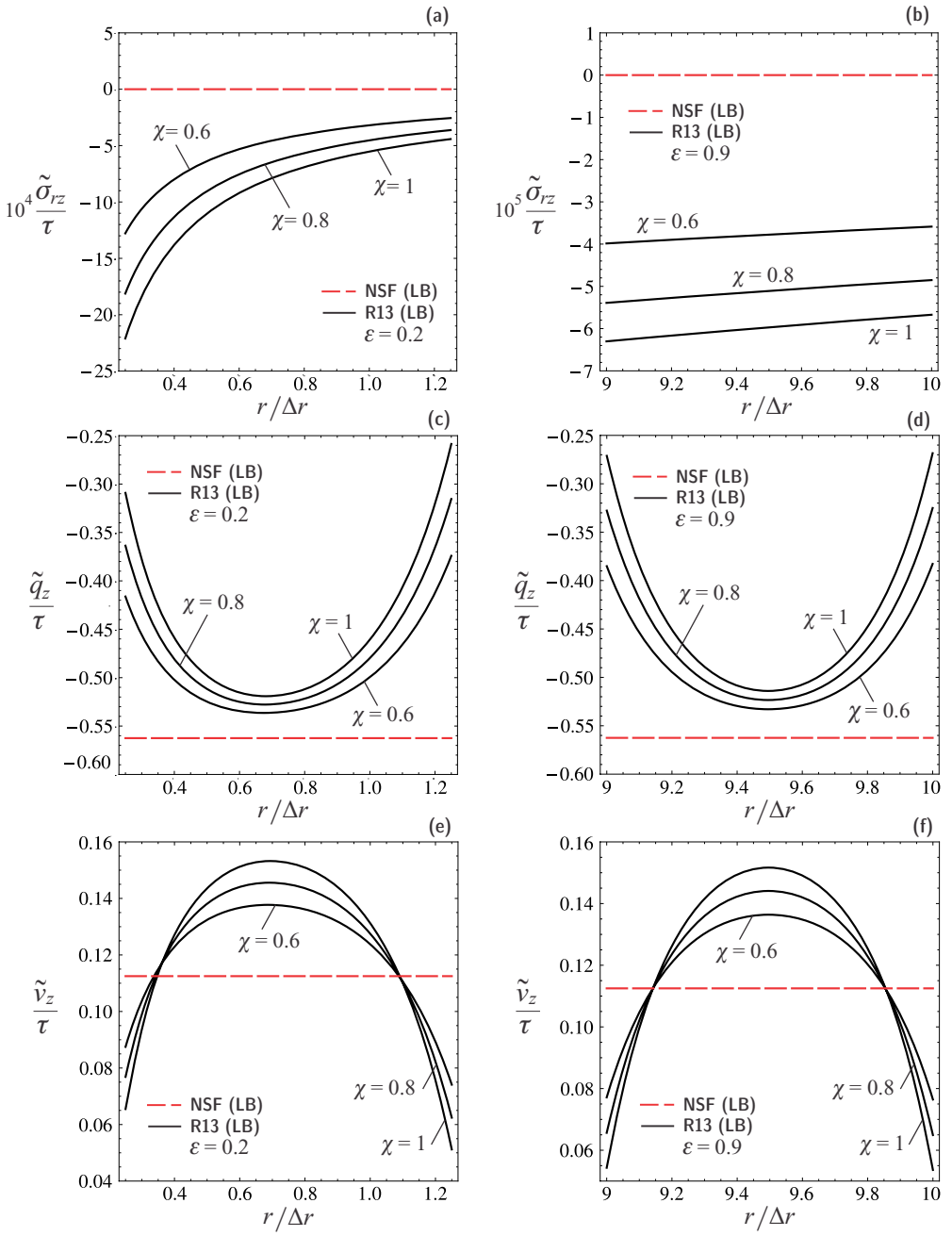

FIG. 3. (Color online) Normalized distributions of (a) and (b) shear stress, (c) and (d) heat flux, and (e) and (f) velocity across the annulus are compared between the NSF and the R13. The plots are obtained for Kn = 0.15, $\chi = \{0.6,0.8,1\}$, and $\varepsilon = \{0.2,0.9\}$ with LB coefficients.

by the LB model is considerably larger than the BGK model, mainly due to the difference in Prandtl numbers. Kinetic data for heat flux are not available for comparison. The validity of our heat-flux solutions are discussed in the next section where the thermal energy flow rate is evaluated from NSF and R13 solutions and is compared to kinetic data.

Figure 2(c) shows the velocity profiles. Similar to heat flux, velocity distribution is uniform in the NSF solution. The term $C_1 \ln(\tilde{r})/\mathrm{Kn}$ in Eq. (34), which represents asymmetric velocity distribution due to curvature effects, vanished in the NSF solution because $C_1 = 0$. The validity of the R13 velocity solution and the effects of the Knudsen layers contribution are discussed in the next section where the mass flow rate is evaluated from NSF and R13 solutions and is compared to kinetic data.

To show the influence of the annulus aspect ratio and the surface accommodation coefficient on the process, solutions for Kn = 0.15, $\varepsilon = \{0.2,0.9\}$, and $\chi = \{0.6,0.8,1\}$ are plotted in Fig. 3. For the plots, the LB coefficients in Eq. (10) are employed. For $\varepsilon = 0.2$, i.e., plots (a), (c), and (e) in Fig. 3, the curvature difference between the inner and the outer walls is significant, and R13 profiles are asymmetric with respect to the centerline of the annulus. For larger values of ε, when the size of the gap decreases and surface curvatures become close, the curvature difference effects vanish, and solutions converge to the planar geometry results [44]. As shown in plots (b), (d),

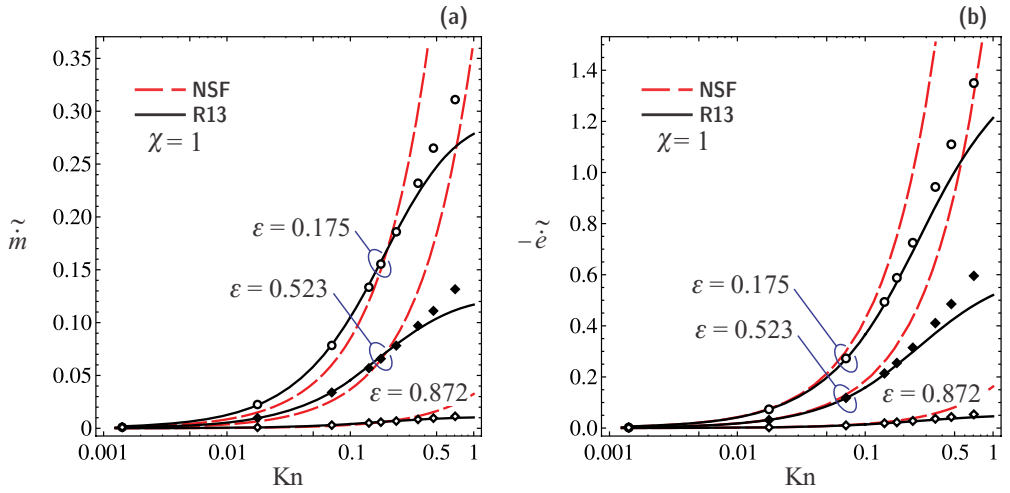

FIG. 4. (Color online) Variations in (a) dimensionless mass flow rate $\tilde{m}$ and (b) dimensionless heat flow rate $\tilde{e}$ with respect to the Knudsen number are shown for $\chi = 1$ and $\varepsilon = \{0.175, 0.523, 0.872\}$. R13 and NSF results are compared to kinetic data from linearized Boltzmann model [47]: symbols.

and (f), for $\varepsilon = 0.9$, the stress distribution converges to a linear distribution (with very small magnitudes), and heat flux and velocity distributions are almost symmetric. Fully dissuasive walls with $\chi = 1$ exhibit more friction, hence, at the walls, stress increases with χ, but heat flux and velocity decrease.

B. Mass and thermal energy flow rates: Comparison with kinetic data

Following the paper of Lo *et al.* [47], flow rates for mass $\dot{m}$ (kg s^{-1}) and heat $\dot{e}$ (J s^{-1}) in transpiration flow can be expressed by phenomenological laws (for the linear case),

$$\dot{m} = F_m \tilde{J}_m, \qquad \dot{e} = F_e \tilde{J}_e, \tag{36}$$

where F_m and F_e are the thermodynamic forces for mass and heat transfer, respectively, and $\tilde{J}_m$ and $\tilde{J}_e$ are the corresponding dimensionless thermodynamic fluxes of mass and heat. The thermodynamic forces, which include the temperature gradient, are [47]

$$F_m = -2\sqrt{2}\pi\mathcal{L}^3 \frac{\rho_0}{\sqrt{\theta_0}} \frac{\partial\theta}{\partial z}, \qquad F_e = -2\sqrt{2}\pi\mathcal{L}^3 \frac{p_0}{\sqrt{\theta_0}} \frac{\partial\theta}{\partial z}, \tag{37}$$

where $\mathcal{L}$ is an arbitrary length. The dimensionless fluxes read

$$\tilde{J}_m = \int_{\tilde{r}_i}^{\tilde{r}_o} \tilde{v}_z \tilde{r}\, d\tilde{r}, \qquad \tilde{J}_e = \int_{\tilde{r}_i}^{\tilde{r}_o} \tilde{q}_z \tilde{r}\, d\tilde{r}, \tag{38}$$

For the sake of consistency with Ref. [47], we set $\mathcal{L} = r_o/\tilde{r}_0$ in Eq. (37) and $\ell = r_o$ in Eq. (24). After straightforward manipulation, dimensionless mass and heat flow rates can be obtained from Eq. (36) as

$$\tilde{m} = -\frac{2\dot{m}}{\pi r_o^2 \rho_0 \sqrt{2\theta_0}\tau} = \frac{4}{\tilde{r}_o^3} \int_{\tilde{r}_i}^{\tilde{r}_o} \tilde{v}_z \tilde{r}\, d\tilde{r}, \tag{39}$$

$$\tilde{e} = -\frac{2\dot{e}}{\pi r_o^2 p_0 \sqrt{2\theta_0}\tau} = \frac{4}{\tilde{r}_o^3} \int_{\tilde{r}_i}^{\tilde{r}_o} \tilde{q}_z \tilde{r}\, d\tilde{r}. \tag{40}$$

In the kinetic simulations [47], a rarefaction parameter δ is defined, that is related to our definition of the Knudsen number [cf. Eq. (25)] via $\delta = 1/(\sqrt{2}\mathrm{Kn})$.

In Fig. 4, variations in dimensionless mass flow rate $\tilde{m}$ and heat flow rate $\tilde{e}$ with respect to the Knudsen number are plotted for $\chi = 1$ and $\varepsilon = \{0.175, 0.523, 0.872\}$. NSF and R13 results are compared to kinetic data from the LB model [47], shown by symbols. As expected, both mass and heat flow rates increase when the diameter of the inner cylinder decreases since larger values for ε correspond to narrower annuli. The solution for a cylindrical tube [12] can be obtained for $\varepsilon \to 0$ (not shown here). As depicted, R13 accurately predicts mass and heat flow rates for $\mathrm{Kn} \leqslant 0.5$, whereas, the NSF fails to follow the kinetic data for the mass flow rate. The NSF results are acceptable only for the heat flow rate at small Knudsen numbers, i.e., $\mathrm{Kn} < 0.07$. At $\mathrm{Kn} = 0.5$, the error of the R13 results with respect to kinetic data, evaluated from error = (data − model)/model, is about 7% for the mass flow rate and 10% for the heat flow rate.

As suggested by the analytical solutions, Eqs. (32)–(34), the presence of Knudsen boundary layers in the R13 solutions besides its accurate boundary conditions are the main reasons for the priority of the R13 over the NSF system.

More comparison is performed in Fig. 5 where the dimensionless mass and heat flow rates from both BGK and LB kinetic models [47] are compared to our macroscopic results for narrow and wide annuli $\varepsilon = \{0.175, 0.872\}$ with $\chi = 1$. In the transition regime where $\mathrm{Kn} < 1$, our results agree with the trend in the kinetic data. Compared to the BGK model, the LB model yields higher values for $\tilde{m}$ and $\tilde{e}$ because velocity and heat flux have larger magnitudes in the LB predictions, see Fig. 2.

VII. CONCLUSION

A compact analytical model based on the R13 equations was employed to describe thermal transpiration flow of rarefied gases in tubes with annular cross sections. Thermally driven flows, forced by small temperature gradients, were investigated with linearized equations where their solutions linearly depend on the temperature gradient. The effects of gas rarefaction,

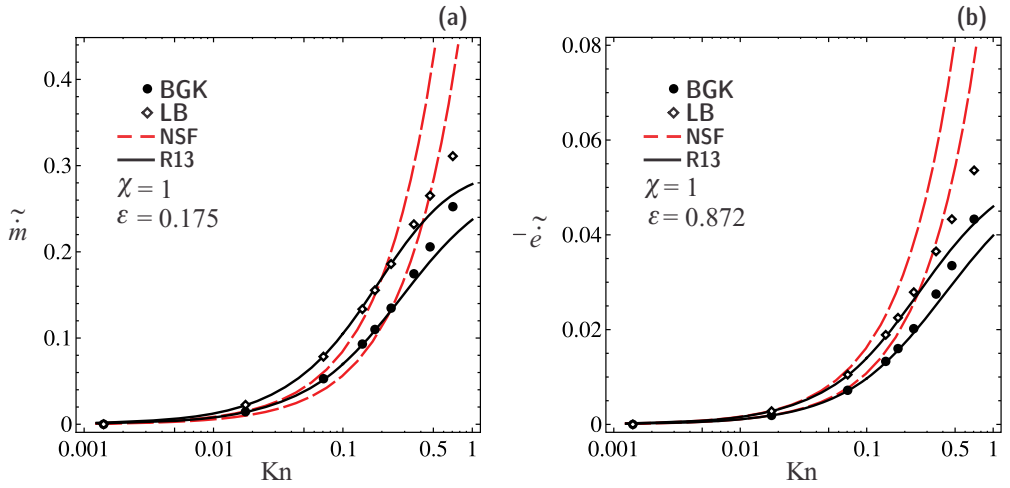

FIG. 5. (Color online) Variations in (a) dimensionless mass flow rate $\tilde{m}$ and (b) dimensionless heat flow rate $\tilde{e}$ with respect to the Knudsen number are shown for $\chi = 1$ and $\varepsilon = \{0.175, 0.872\}$. R13 and NSF results are compared to kinetic data from linearized Boltzmann model: diamonds, and BGK model: circles. Kinetic data are borrowed from Ref. [47].

annulus geometry, and surface accommodation on the solutions of shear stress, heat flux, and velocity were examined.

Comparison of R13 solutions with kinetic data revealed that the dominant rarefaction effects in the considered flow were as follows: (i) formation of the Knudsen boundary layers and (ii) slip velocity on the walls. The effects of these nonequilibrium phenomena on mass and heat flow rates are thoroughly demonstrated and are compared to high-quality Boltzmann solutions as experimental measurements for this problem are not reported. The presented comparisons with kinetic solutions confirm that the R13 system successfully predicts mass and heat transfers for $\mathrm{Kn} < 0.5$ with errors below 7% for the mass flow rate and below 10% for the heat flow rate.

By comparing NSF and R13 solutions, it is evident that Knudsen layers and their contribution on velocity slip are absent in the NSF theory; this is where the real advantage of the R13 stands out. We highlighted the consequence of these shortcomings in the NSF equations by computing mass and heat flow rates and showed that the NSFs were valid in the slip flow regime only.

To conclude, we point to the insufficiency of the R13 equations for the description of highly rarefied flows in which the magnitude of rarefaction effects is beyond the resolution of the R13 equations. In such conditions, larger systems of moment equations [51] are suggested. As demonstrated in Ref. [39], higher-order linearized moment systems lead to solutions with multiple Knudsen layers, and their superposition provides a more accurate structure for the Knudsen layers. The authors agree that solutions of large moment systems can be computationally as expensive as kinetic solutions, specifically, full numerical solutions. Indeed, the derivation of analytical solutions is a cumbersome task too, particularly, in curvilinear coordinates; however, it needs to be performed once. Analytical solutions are continuous in the independent variables and show explicitly how the parameters of the system are involved. Also, analytical solutions give much insight into the underlying physics, which is one of the primary objectives of modeling.

ACKNOWLEDGMENT

P.T. thanks Dr. H. Struchtrup (University of Victoria, Canada) for many helpful discussions. Financial support of the Natural Sciences and Engineering Research Council of Canada (NSERC) is greatly appreciated.

[1] Y. Sone, Annu. Rev. Fluid Mech. **32**, 779 (2000).
[2] Y. Sone, *Kinetic Theory and Fluid Dynamics* (Birkhäuser, Boston, 2002).
[3] O. Reynolds, Philos. Trans. R. Soc. London **170**, 727 (1879).
[4] C. Maxwell, Philos. Trans. R. Soc. London **170**, 231 (1879).
[5] M. Knudsen, Ann. Phys. **31**, 205 (1910).
[6] M. Knudsen, Ann. Phys. **33**, 205 (1910).
[7] S. C. Liang, J. Appl. Phys. **22**, 148 (1951).
[8] T. Takaishi and Y. Sensui, Trans. Faraday Soc. **59**, 2503 (1963).
[9] T. Edmonds and J. P. Hobson, J. Vac. Sci. Technol. A **2**, 182 (1965).
[10] R. A. Watkins, W. L. Taylor, and W. J. Haubach, J. Chem. Phys. **46**, 1007 (1967).
[11] B. T. Porodnov, A. N. Kulev, and F. T. Tukhvetov, J. Fluid Mech. **88**, 609 (1978).
[12] P. Taheri and H. Struchtrup, Phys. Fluids **22**, 112004 (2010).
[13] S. E. Vargo, E. P. Muntz, G. R. Shiflett, and W. C. Tang, J. Vac. Sci. Technol. A **17**, 2308 (1999).
[14] Y.-L. Han, E. P. Muntz, A. Alexeenko, and M. Young, Nanoscale Microscale Thermophys. Eng. **11**, 151 (2007).
[15] D. C. York, A. Chambers, A. D. Chew, and A. P. Troup, Vacuum **55**, 133 (1999).
[16] H. Struchtrup, *Macroscopic Transport Equations for Rarefied Gas Flows: Approximation Methods in Kinetic Theory* (Springer, New York, 2005).
[17] S. K. Loyalka, J. Chem. Phys. **55**, 4497 (1971).
[18] S. K. Loyalka, Phys. Fluids **17**, 1053 (1974).

[19] S. K. Loyalka, J. Chem. Phys. **63**, 4054 (1975).
[20] S. K. Loyalka, N. Petrellis, and T. S. Storvick, Z. Angew. Math. Phys. **30**, 514 (1979).
[21] L. B. Barichello, M. Camargo, P. Rodrigues, and C. E. Siewert, Z. Angew. Math. Phys. **52**, 517 (2001).
[22] T. Ohwada, Y. Sone, and K. Aoki, Phys. Fluids A **1**, 2042 (1989).
[23] S. K. Loyalka and K. A. Hickey, J. Vac. Sci. Technol. A **9**, 158 (1991).
[24] Y. Sone and K. Yamamoto, Phys. Fluids **11**, 1672 (1968).
[25] S. K. Loyalka, Phys. Fluids **12**, 2301 (1969).
[26] B. T. Porodnov and F. T. Tukhvetov, J. Eng. Phys. Thermophys. **36**, 61 (1979).
[27] S. S. Lo, S. K. Loyalka, and T. S. Storvick, J. Chem. Phys. **81**, 2439 (1984).
[28] D. Valougeorgis and J. R. Thomas, Phys. Fluids **29**, 423 (1986).
[29] F. Sharipov, J. Vac. Sci. Technol. A **14**, 2627 (1996).
[30] C. E. Siewert, J. Comput. Phys. **160**, 470 (2000).
[31] F. Sharipov, Eur. J. Mech. B/Fluids **22**, 145 (2003).
[32] F. Sharipov and V. Seleznev, J. Phys. Chem. Ref. Data **27**, 657 (1998).
[33] H. Struchtrup and P. Taheri, IMA J. Appl. Math. **76**, 672 (2011).
[34] H. Grad, Commun. Pure Appl. Math. **2**, 325 (1949).
[35] H. Grad, in *Handbuch der Physik XII: Thermodynamik der Gase*, edited by S. Flugge (Springer, Berlin, 1958).
[36] S. Chapman and T. G. Cowling, *The Mathematical Theory of Non-uniform Gases* (Cambridge University Press, Cambridge, 1970).
[37] H. Struchtrup and M. Torrilhon, Phys. Fluids **15**, 2668 (2003).
[38] H. Struchtrup, Phys. Fluids **16**, 3921 (2004).
[39] X.-J. Gu, D. R. Emerson, and G.-H. Tang, Phys. Rev. E **81**, 016313 (2010).
[40] M. Torrilhon and H. Struchtrup, J. Fluid Mech. **513**, 171 (2004).
[41] P. Taheri, M. Torrilhon, and H. Struchtrup, Phys. Fluids **21**, 17102 (2009).
[42] P. Taheri, A. S. Rana, M. Torrilhon, and H. Struchtrup, Continuum Mech. Thermodyn. **21**, 423 (2009).
[43] P. Taheri and H. Struchtrup, Phys. Rev. E **80**, 066317 (2009).
[44] P. Taheri and H. Struchtrup, Physica A **389**, 3069 (2010).
[45] P. Taheri and H. Struchtrup, Int. J. Heat Mass Transf. **55**, 1291 (2012).
[46] M. Torrilhon and H. Struchtrup, J. Comput. Phys. **227**, 1982 (2008).
[47] S. S. Lo, S. K. Loyalka, and T. S. Storvick, J. Vac. Sci. Technol. A **1**, 1539 (1983).
[48] P. Taheri, Ph.D. thesis, University of Victoria, 2010.
[49] M. Torrilhon, Phys. Fluids **22**, 072001 (2010).
[50] H. Struchtrup and M. Torrilhon, Phys. Rev. E **78**, 046301 (2008).
[51] X. Gu and D. R. Emerson, J. Fluid Mech. **636**, 177 (2009).